Experimental Evidence of the Feeding of the Free Troposphere with Aerosol Particles from the Mixing Layer

Evelyn Freney, Karine Sellegri, Eija Asmi, Clémence Rose, Aurélien Chauvigné, Jean-Luc Baray, Aurélie Colomb, Maxime Hervo, Nadège Montoux, Laëtitia Bouvier, et al.

Aerosol and Air Quality Research, 16: 702–716, 2016

ISSN: 1680-8584 print / 2071-1409 online
doi: 10.4209/aaqr.2015.03.0164

Experimental Evidence of the Feeding of the Free Troposphere with Aerosol Particles from the Mixing Layer

Evelyn Freney[1,2*], Sellegri Karine[1,2], Asmi Eija[3], Rose Clemence[1,2], Chauvigne Aurelien[1,2], Baray Jean-Luc[1,2], Colomb Aurelie[1,2], Hervo Maxime[4], Montoux Nadege[1,2], Bouvier Laeticia[1,2], Picard David[1,2]

[1] *Clermont Université, Université Blaise Pascal, OPGC, Laboratoire de Météorologie Physique, BP 10448, 63000 Clermont-Ferrand, France*
[2] *CNRS, UMR6016, LaMP/OPGC, BP80026, 63177 Aubière, France*
[3] *Finish meteorological institute, Helsinki, Finland*
[4] *Federal Office of Meteorology and Climatology, MeteoSwiss, Payerne 1530, Switzerland*

ABSTRACT

Aerosol particles emitted by both natural and anthropogenic sources have direct and indirect radiative impacts. Within the planetary mixing layer (ML), these particles are subjected to a large number of removal processes, e.g., rain, sedimentation, coagulation, and thus have a relatively short lifetime. Once aerosols are transported into the free troposphere (FT), their atmospheric lifetime increases significantly and they tend to be representative of large spatial areas. The work presented here shows evidence of anthropogenic emissions being transported from the ML to the FT during a cold period in February 2012. Using a wide range of in-situ measurements of aerosol chemical and physical properties at the Puy de Dome (PUY) station, as well as LIDAR measurements (at the Cezeaux site) of atmospheric back scattering we studied the exchange between the ML and the FT. Criteria used to identify when the PUY station was sampling in the ML or in the FT included mixing layer height estimates from LIDAR measurements, trace gas measurements, and air mass trajectories. Within the FT, we observed a gradual change in aerosol physical properties with increases in aerosol mass concentrations of up to 2 times the starting concentration, as well as increases in the number of larger particles (particle diameter >150 nm). Aerosol chemical properties showed increases in organic and nitrate particles. A series of linear fits were made through the data providing information on how different parameters change as a function of time. The impact of these changing aerosol properties are discussed in relation to the potential influence on aerosol direct and indirect effects. This work presents a unique combination of observations, and provide valuable data for future model validation.

Keywords: Long-range transport; Aerosol Mass Spectrometry; High altitude site.

INTRODUCTION

As a result of the large uncertainties associated with their direct and indirect radiative effects, aerosol particles have received increasing attention over the last decade (IPCC, 2013). The direct effects include the radiative scattering and absorption of aerosol particles related to their size and composition, and indirect effects include the radiative scattering and absorption of aerosol particles after they interact with atmospheric water vapour to form cloud droplets (McFiggans *et al.*, 2006). Both effects are dependent on the aerosol chemical composition, size distribution, and number concentration. However, the magnitude of these direct and indirect effects is determined by both the horizontal and vertical distribution of aerosol particles in the atmosphere (Laj *et al.*, 2009).

Aerosol particles, emitted naturally and anthropogenically into the atmosphere, are most concentrated in the atmospheric mixing layer (ML), where they are subjected to several removal processes from rain, particle coagulation, or sedimentation. In the free troposphere (FT), aerosol particles are subjected to fewer removal processes and therefore have longer lifetimes, allowing them to be transported or recirculate regionally over several days, therefore increasing their impact on the climate. Under favourable atmospheric conditions, aerosol particles transported into the FT can be re-entrained back into the ML, affecting the air quality several thousands of kilometres from the source region (McKendry *et al.*, 2001, Timonen *et al.*, 2013). In addition

* Corresponding author.
E-mail address: e.freney@opgc.univ-bpclermont.fr

to the impacts on aerosol direct effects, conditions suitable for the activation of aerosol particles into cloud droplets occur more often in the FT than in the ML. For these reasons, measurements characterising the composition and physical properties of aerosol particles and gas-phase species in the FT are important for the validation of global transport and satellite retrieval models (Martin *et al.*, 2004).

Several airborne studies have highlighted the strong contribution from organic and sulphate aerosol particles in the FT (Heald *et al.*, 2006; Murphy *et al.*, 2006; Crumeyrolle *et al.*, 2013). Sulphate particles in the FT can be formed from the OH oxidation of gas-phase SO_2. However, the formation mechanisms of organic aerosols (OA) in the FT are less well documented. Heald *et al.* (2005) proposed that the large and maintained source of OA particles is related to secondary aerosol formation from volatile organic compounds from either natural or anthropogenic sources transported from the ML. These observations are in agreement with studies showing that air masses transported from the ML can favour new particle formation in the FT (Twohy *et al.*, 2002; Rose *et al.*, 2015). Henne *et al.* (2004) described events where long-range transported anthropogenic emissions have been identified on the Jungfraujoch research station, as well as events where slope winds contribute to the transportation of urban emissions from the ML into the FT.

The principal reasons for interactions between the ML and the FT layers can be from synoptic systems, deep and shallow cumulus, and dry convection (Fiedler, 1982). Slope/valley winds in mountainous areas (Henne *et al.*, 2004) turbulence and vertical exchange all play central roles in the interactions between the ML and FT (McKendry and Lundgren, 2000). In addition, periods of heavy pollution or photochemical smog are generally associated with anti-cyclonic conditions. A number of studies have used numerical simulations to investigate the transport of pollutants from the ML to the FT, identifying convection and vertical advection (Hov and Flatoy, 1997) as some of the most important processes. However, the role of cold fronts over polluted areas can result in the rapid transport of pollutants to the FT (Chaumerliac *et al.*, 1992; Donnell *et al.*, 2001).

This work presents a series of in-situ measurements of aerosol and gas-phase properties at the Puy de Dome (PUY) mountain research site during a winter sampling period. Complementary measurements of atmospheric back scattering were available from LIDAR measurements. We use this combined data to quantify the influence of regional and long-range transported emissions on the physical and chemical properties of the FT aerosol over a number of days. After describing the instrumental measurements and meteorological conditions encountered during this experiment, we define our criteria for choosing both the ML and FT periods. We then discuss the properties of the aerosol particles within the ML, and in the FT at the start of the sampling period, followed by a description of how these properties change as a function of time. The discussion is concluded with a description of how these changes in aerosol particles influence aerosol direct and indirect effects.

MATERIAL METHODS

The Research Site

The global atmospheric watch (GAW) PUY research station is situated in central France (45°460 N, 2°570 E) at an altitude of 1465 m a.s.l. It is one of the 21 stations within the ACTRIS aerosol monitoring program and is classified as a background regional site (Asmi *et al.*, 2011). The site is surrounded by fields and small villages and the nearest large city, Clermont Ferrand is situated 16 km to the east of the station. There is no public road access to the site. A second sampling site (Cezeaux (CZ)) is situated on the University campus south of the city of Clermont Ferrand at 410 m a.s.l.

At both sites, meteorological properties are measured on a continuous basis including wind direction, wind speed, relative humidity (RH), pressure, and temperature. At the PUY site, size segregated aerosol number concentration is measured using a scanning mobility particle sizer (SMPS), sampling particles with diameters from 17 nm up to 450 nm. Aerosol particle chemical composition was measured using a compact time of flight mass spectrometer (C-ToF-AMS). Black carbon (BC) measurements are performed using a Multi Angle Absorption Photometer (MAAP 5012) at a wavelength of 637 nm. Gas-phase species such as SO_2, CO, CO_2, O_3, NO, and NO_2 are also measured throughout the year. At the CZ site, a LIDAR was measuring atmospheric back scattering continuously providing information on the vertical profile of the aerosol concentration with a resolution of approximately 10 minutes.

C-ToF-AMS + BC

Submicron aerosol particle composition was measured using a C-ToF-AMS (Aerodyne, Drewnick *et al.*, 2005). This instrument samples aerosol particles with aerodynamic diameters ranging from approximately 80 nm up to ~800 nm. The instrument is capable of sampling inorganic species such as sulphate (SO_4), nitrate (NO_3), ammonia (NH_4), chloride (Cl) and organic (Org) aerosol compounds. A time resolution of ~5 minutes was chosen for this study.

The C-ToF-AMS data needs to be corrected for particle losses due to non-spherical particles or as a result of particle bounce off the vapourizer. This is done by applying a collection efficiency (CE) factor to the raw C-ToF-AMS data. It has recently been shown that particles containing high fractions of nitrate or sulphate aerosol are more efficiently sampled than other aerosol particles and therefore composition dependant CEs must be applied (Middlebrook *et al.*, 2012). During this study, there were often significant contributions from nitrate particles, as well as periods that were identified as being acidic. The acidity of the aerosol is determined by comparing the ratio of the measured NH_4 (NH_{4MEAS}) to that predicted from the measured concentrations of SO_4, NO_3, and Cl species, if all compounds existed as $(NH_4)_2SO_4$, NH_4NO_3, and NH_4Cl (neutralised aerosol). If the ratio (NH_{4MEAS}:NH_{4PRED}) is lower than 0.70, there is likely excess SO_4 in the form of $NH_4(HSO_4)$ resulting in an acidic aerosol. These correction procedures are now included in the new versions of the IGOR software program, Squirrel (1.53C) which were used for the analysis of this data. The

composition dependent CE ranged from 0.5 up to 0.99. Once the CE was applied, the C-ToF-AMS mass concentrations were converted to volume concentrations using densities of 1.75 g cm^{-3} for inorganic species, and 1.3 g cm^{-3} for organic species. The C-ToF-AMS volume concentration was combined with that of BC (density of 1.8 g cm^{-3}) and compared with the volume concentration measured by the SMPS, sampling behind the same inlet. This comparison provided good agreement between the two instruments with an R^2 of 0.83 and a slope of 0.96. Varying the organic density between 1.2 g cm^{-3} and 1.4 g cm^{-3} varied this slope from 0.94 to 0.98, respectively. The lower correlation is a result of some periods when the SMPS measured higher concentrations than the C-ToF-AMS. This is possibly a result of refractory aerosol particles not sampled by the C-ToF-AMS.

The C-ToF-AMS instrument was calibrated prior to and after the campaign period using size selected (300 nm) ammonium nitrate particles. The relative ionization efficiency and the ionization efficiency were 3.66 and 2.4 × 10^{-7}, respectively. Particle free air was sampled for a duration of 5 minutes once every four days in order to make the necessary adjustments to the mass spectra fragmentation table.

Positive Matrix Factorisation (PMF) Analyses

Positive matrix factorisation (PMF) was applied to the raw organic mass spectra acquired from the C-ToF-AMS. PMF analysis uses a combination of organic aerosol mass spectral profiles together with their temporal evolutions to identify contributions from different types (factors) of organic species (Ulbrich *et al.*, 2009). The optimal number of factors extracted from the PMF solution was determined by comparing the correlations of the factor time series and mass spectral profiles with external time series and reference mass spectra. A four factor solution with an fpeak value of 0 (fpeak is a parameter describing the rotation of the PMF matrix solution) was chosen to best represent the organic aerosol data at the PUY station (Figs. S2–S6. Extending the PMF solution to five variables did not show any improvement in the correlations nor any improvement in the residuals (Fig. S3). All full list of all correlation with external species (Tables S1 and S2) and with reference mass spectra (Table S3) are available in the supplementary material.

Separating four factors at the PUY site is rare with unconstrained PMF analysis, since the organic aerosol is usually very well mixed and oxidised when it arrives at the site (Freney *et al.*, 2011; Crippa *et al.*, 2014). This shows that there was an exceptional variation of organic aerosols species encountered during this period. The four different organic particle types included a primary/hydrocarbon organic aerosol (HOA), strongly correlating with reference HOA mass spectra (Pearson's r correlation (P_R) = 0.98), and three types of oxidised organic aerosols (OOA). These resolved OOA mass spectra had maximum Pearson's R correlations with reference mass spectra (taken from Crippa *et al.*, 2014) of 0.83 (low volatile OOA (LV-OOA)), 0.68 (Biomass burning (BBOA)), and 0.68 (Semi-volatile OOA (SV-OOA)) (Table S3). These resolved organic aerosols will be referred to as LV-OOA, BBOA, and SV-OOA, respectively. The resolved mass spectra of both LV-OOA and SV-OOA were similar, however their temporal evolution was different enough that we chose to keep the four factor solution. The LV-OOA and SV-OOA species are correlated with secondary species such as SO_4 (Pr = 0.95, Pr = 0.89). The BBOA factor had the highest correlations with m/z 60 (Pr = 0.96) and m/z 73 (Pr = 0.94) compared with the other resolved organic factors. More detailed discussion on the temporal evolution and contribution of the resolved organic aerosol species will be provided later in the discussion.

Gas-Phase Measurements: VOC + Other Online

Gaseous compounds were sampled using a Teflon sampling line with a time resolution of 5 minutes. Measurements of SO_2 were performed online with a Thermo Environmental Instruments (TEI) Model 43C–TLE using UV fluorescence technology. Measurements of carbon monoxide (CO) were performed with the TEI Model 48i-TLE CO Analyzer, which utilizes infra-red technology. NO_x was measured using TEI 42-TLE using ozone chemiluminescence technology. NO_Y measurements were performed with a TEI model 42CY using chemiluminescent detection.

Additional off-line measurements of volatile organic carbon (VOC) species were made using a SASS (Smart automatic Sampling System (TERA Environment)), with a resolution of three hours. Gaseous compounds were sampled at 100 mL min^{-1} into a multi-sorbent cartridge composed of Tenax TA 60-80 mesh (250 mg) and carbosieve sIII (150 mg). The two adsorbants were separated by stainless steel grids. Prior to the sampling, the multi-sorbent filled cartridges were conditioned with purified air at a flow rate of 30 mL min^{-1}, for 4 hours. This type of cartridge allowed sampling of C_4–C_{14} aromatic compounds, n-alkanes, monoterpenes, isoprene, and halogenated compounds. These cartridges were subsequently analysed using a gas chromatograph mass spectrometer system (GC/MS, Perkin Elmer) connected to an automatic thermal desorption.

Optical Measurements: Nephelometer, LIDAR, Photometer

A LIDAR instrument was operating on the roof of the CZ site measuring atmospheric back scattering and therefore providing information on the vertical profile of aerosol particles. The LIDAR instrument is a Raymetrics Rayleigh Mie Raman, emitting at 355 nm, with a spatial resolution of 7.5 m. More detailed descriptions of this instrument are available in Hervo *et al.* (2012) and Freville *et al.* (2015). The LIDAR instrument was used to determine the height of the ML using the wavelength covariance technique (Brooks, 2003). This method is described in detail in Rose *et al.* (2015) and uses the range corrected LIDAR signal. The white area in Fig. 2(a) represent periods where either clouds or dust layers were observed (Fig. S1), making it impossible to use the Rayleigh fit to inverse the raw LIDAR signal over the full vertical profile. In the case where clouds were present at the altitude of the site it is not possible to calculate the mixing layer height (MLH), however for periods when dust or clouds were present at high altitudes it was still possible to calculate the MLH (Fig. S1). Using LIDAR

measurements we can determine the aerosol optical depth (AOD) at 355 nm. In order to do this, aerosol backscattering coefficient profiles (β_{LIDAR}) are retrieved using Fernald-Klett inversion (Klett, 1981; Matthais *et al.*, 2004) and applied to the LIDAR range corrected signal (Pr^2 signal) using a specific LIDAR ratio (LR) of 58sr (Müller *et al.*, 2007). The signal obtained from the LIDAR is valid between 800 m and 7 km. However, in order to calculate the AOD within the FT, the LIDAR extinction profile (EXT_{LIDAR}) is integrated over altitudes (z) between 2 km and 5 km ($AOD_{2\text{-}5km}$) (Eqs. (1) and (2)).

$$AOD_{LIDAR}^{FT} = \int_{2}^{5km} Ext_{LIDAR} \cdot dz \quad (1)$$

$$Ext_{LIDAR} = \beta_{LIDAR}.LR \quad (2)$$

Integral values of LIDAR measurements from the ground up to altitudes of 5 km has been shown to be representative of the total atmospheric column and has been validated with aircraft measurements, where AOD calculated from airborne extinction measurements were compared with AOD calculated using a photometer on the ground (Nicolas *et al.*, in prep). It is therefore considered that any contribution above 5 km is thought to be very weak. A lower altitude of 2 km was used to ensure that we were measuring atmospheric properties within the FT. These calculations are only valid during FT sampling periods (Fig. 2).

The in-situ total and back scattering properties of atmospheric particles at the PUY site were measured by a three wavelength (450, 550, and 700 nm) nephelometer (TSI 3563). These data were corrected for detection limits and truncation errors according to Anderson and Ogren (1998). The absorption coefficient (σap) was measured by a Multi-angled absorption photometer (MAAP 5012) (Petzold *et al.*, 2005). The upscatter fraction was determined from the asymmetry parameter measured by the nephelometer according to the parametrization in Andrews *et al.* (2006) (Eqs. (3) and (4)). A surface reflectance of 0.16 was used.

$$g = -7.143889b^3 + 7.464439b^2 - 3.96356b + 0.9893 \quad (3)$$

$$\beta_r = \frac{1}{2(1-g)} \quad (4)$$

b is the ratio between total and backscattering measured by the nephelometer.

Back Trajectory Analysis

Groups of back-trajectories have been computed using LACYTRAJ, a three-dimensional kinematic trajectory code using dynamical fields produced by the ECMWF (Clain *et al.*, 2010). In this work we use ERA-Interim reanalyses with a horizontal resolution of 0.75° in latitude and longitude, and 37 vertical levels. Each grid point is advected using a bilinear interpolation for horizontal wind fields and time and a log-linear interpolation for vertical wind field. These trajectories are calculated every 15 minutes for 96 hours of back-trajectories, for each day of the experiment with a starting height of 1465 m a.s.l. The resulting trajectories were then classified under one of five possible sources, from oceanic, Mediterranean, continental, northerly, or local, similar to those used in Asmi *et al.* (2012) and Rose *et al.* (2013). The altitude of each trajectory was compared with the calculated height of the mixing layer, interpolated in time and space from ECMWF ERA-Interim, along all trajectory points, in order to determine if the air mass interacted with the mixing layer (Fig. 1).

RESULTS

Characterisation of Meteorology, Back Trajectories

The sampling period started on the 15th of January and continued until the 13th of February, 2012. For the first week of the experiment, oceanic air masses arrived at the site. Average temperatures were 0°C ± 2°C, and there were several cloud events. From the 5th of February onwards, cold and dry air masses arrived from the continent. During the cold event, temperatures were as low as –18°C. According to Britain's Met Office, the cold weather was the result of a large area of high pressure over Eastern Europe resulting in exceptionally cold temperatures over a large area of Europe. During this cold event, electricity usage records were broken in France and several other countries in Europe. Hydro-electric dams were opened and several gas and coal stations were also brought back into use to provide the needed electricity, (http://ec.europa.eu/energy/observatory/electricity/doc/qreem_2012_quarter1.pdf). This pollution event was observed at other atmospheric measurement sites in France, where significant increases in aerosol concentrations, notably anthropogenic aerosols were observed during the month of February (Petit *et al.*, 2015).

Defining Mixing Layer and Free Troposphere Measurements

Using LIDAR measurements to calculate the MLH, we were able to define time periods when the PUY research site was sampling in the FT or in the ML. The ML is defined as a part of the lower troposphere that is directly influenced by emissions from the surface and can include aerosol particles from both anthropogenic and natural sources. Particle concentrations are normally highest in this part of the atmosphere. Directly above the ML, is entrainment zone (EZ). The EZ is a stable layer above the ML and acts as a barrier to rising turbulence and hence inhibits turbulence (Stull, 1988). Above the EZ is the FT, where aerosol concentrations are lowest. As EZ show intermediate properties between ML and FT over a restricted layer height, we chose not to discuss them further and focused on the properties of the FT.

Using LIDAR measurements we were able to calculate the MLH (Fig. 2(a)). Fig. 2(a) shows the inverted extinction profiles from 800 m to 2500 m. The white periods represent periods where clouds or dust layers were present at high altitudes, making it impossible to integrate the LIDAR signal over the full vertical profile. However, during these periods the MLH is always lower than cloud height and it

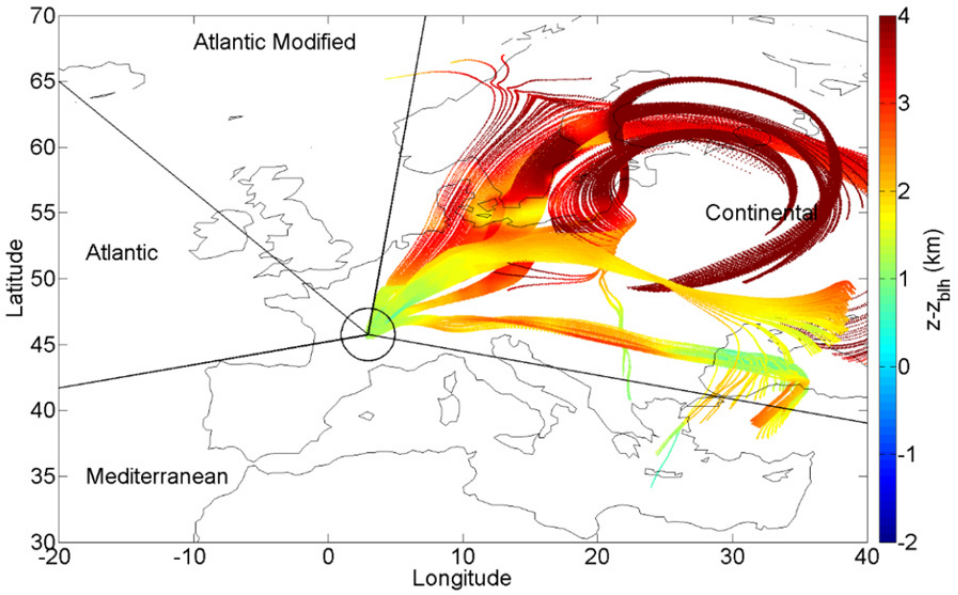

Fig. 1. 96 hr ECMWF backward trajectories for air masses arriving at the PUY site during FT sampling periods during the 5th and 10th of February 2012. The color scale represents the difference between the calculated height (z) of the air mass trajectory and the calculated height of the mixing layer height (z-z_{bln} (km)).

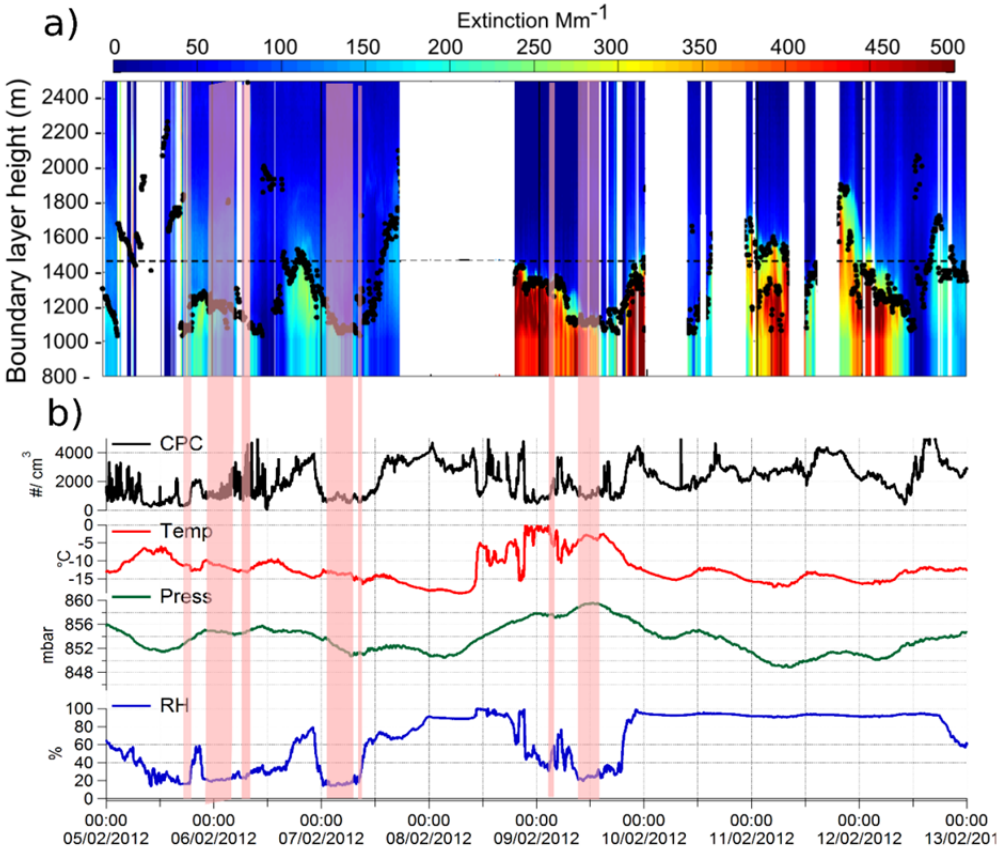

Fig. 2. a) LIDAR vertical profiles measured at the Cezeaux site from the 5th to the 13th of February. Color is the aerosol Extinction at 355 nm black dots are used to illustrate the mixing layer height calculated using the wavelength covariance technique. White areas represent periods when clouds were present at higher altitudes making it impossible to invert the LIDAR signal over the full vertical range of the measurements. b) shows a range of meteorological parameters measured at the site. Red bars indicate when the site is in thought to be in the free troposphere. Periods outside of the red bars correspond to when the site was in the mixing layer or in a residual layer.

was therefore possible to determine a MLH during the entire sampling period. Using the calculated MLH in conjunction with online aerosol and gas phase measurements as well as with meteorological parameters, we identified a number of periods when the site was in the FT, listed in Table S4. The site was considered to be in the FT by using the following criteria: 1) MLH < 1400 m (from LIDAR calculations), 2) a low ratio of NO_Y/CO (< 0.01) (Figs. 2(c) and 3)). If criteria 1) and 2) were satisfied the height of the air mass trajectory with respect to the height of the calculated MLH (ECMWF) was determined for the specific periods (Fig. 1). We are aware that the ECMWF model provides only an indication on the large scale origin of the air masses. The chosen periods of FT sampling (Table S4 were influenced by air masses that spent at least the previous 72 hours in the FT without any direct interaction with mixing layer aerosols (Fig. 1). These air masses were at least 300 m above the mixing layer height for 72 hours. Trajectories between 72 and 96 hours were occasionally reported to be lower than the MLH by 140 m. It should be noted that some of these chosen periods represent FT sampling times of only 40 minutes to 1 hour, while others are as long as 6 hours. For this reason some caution should be taken for the short sampling times (Table S4, no. 5, 6).

The choice of these criteria were then validated by observed changes in aerosol composition (aerosol composition dominated by sulphate and organic aerosols in the FT) (Fig. 3(a)), and a change in aerosol number concentration and size distributions (low number concentrations of accumulation mode aerosol (Fig. 3(b)).

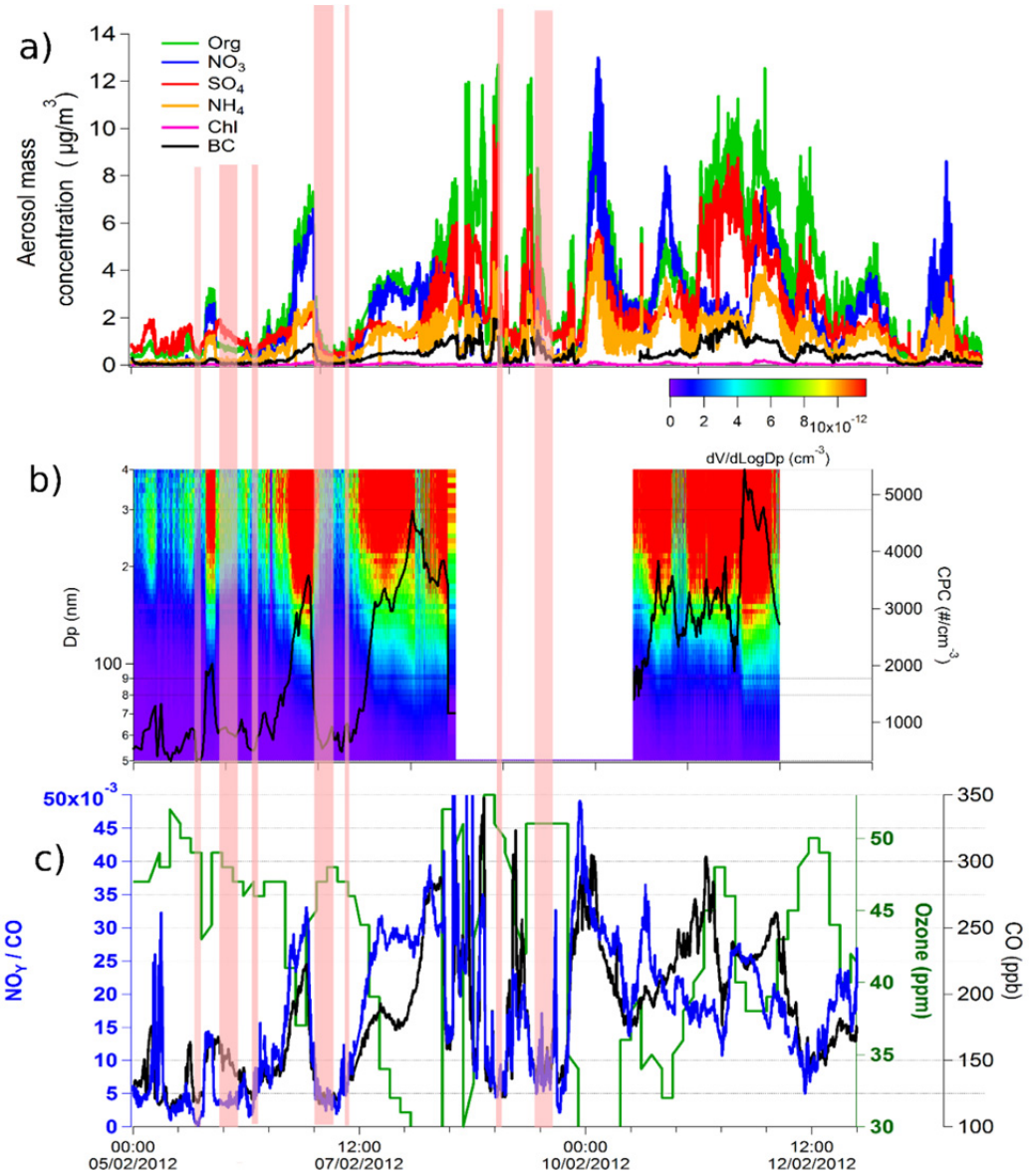

Fig. 3. a) NR-PM1 measured by the C-ToF-AMS and BC (µg m^{-3}) and b) SMPS volume concentrations (dV/dLogDp (cm^{-3})) with particle number concentration measured by a CPC (cm^{-3}), and c) several gas-phase components measured at the site from the 5th of February until the 13th of February. Red bars indicate when the site is in thought to be in the free troposphere. Periods outside of the red bars correspond to when the site was in the mixing layer or in a residual layer.

Aerosol and Gas Properties in the Mixing Layer

Previous studies at the PUY research site have shown that there is a small contribution from fresh anthropogenic emissions at the site during the summer months (Freney *et al.*, 2011). However, during the winter months, when there is an increased consumption of heating fuels and biomass burning, there are often episodes when the measured aerosol contains a high contribution from primary combustion aerosols (Freney *et al.*, 2011; Crippa *et al.*, 2014).

Throughout the sampling period from the 5th to the 13th of February 2012, there were several episodes when the PUY site was within the ML and hence affected by emissions from the surrounding areas (Figs. 2 and 3). In this section, we describe the aerosol physical and chemical properties measured during the first days of sampling in the ML prior to a sustained influence from continental air masses. All values shown are mean values with errors of ± 1σ. Pearsons r (Pr) correlations are calculated only for the first days of sampling in the ML. Aerosol size distributions measured by the SMPS show a single broad size distribution at around 100 ± 30 nm, with high average number concentrations e.g., 4 × 10^3 ± 1 × 10^3 (dN/dLog(Dp) (cm^{-3})) (Fig. 4). Aerosol particle composition was dominated by organic and nitrate aerosol particles having mean values of 4.8 μg m^{-3} ± 2.3 μg m^{-3} and 3.8 μg m^{-3} ± 2.5 μg m^{-3}, respectively (contributing 37% and 28%, respectively to the total aerosol mass). Organic and nitrate aerosol particles correlated well with black carbon (BC) particles (Pr = 0.88 and 0.92, respectively). BC particles measured at the site contributed approximately 5% to the total mass (0.5 μg m^{-3} ± 0.4 μg m^{-3}), this is slightly higher than previous BC measurements (Freney *et al.*, 2011), where concentrations were on average 0.38 μg m^{-3} ± 0.1 μg m^{-3}. Both organic and nitrate aerosol particles had similar correlations with CO (Pr = 0.59 ± 0.01) and NO_x (Pr = 0.49 ± 0.04). Sulphate and ammonia only contributed between 17% and 13%, respectively. SO_4 correlated with Org and NO_3 species (Pr = 0.90 and 0.80, respectively), and with BC (Pr = 0.77), CO (Pr = 0.57), NO_x (Pr = 0.42), suggesting that all species have been transported together from nearby sources. High contributions from ammonium nitrate and organics, and low contributions from ammonium sulphate aerosols within the ML, are typical indicators of air masses that are strongly influenced by anthropogenic emissions.

Of the four different organic factors resolved using PMF, the LV-OOA species contributes 40% ± 10% of the total organic mass, and correlates with secondary species such as SO_4 (Pr = 0.96) (Fig. S2), SV-OOA contributes 20% ± 5%. BBOA contributes up to 30 ± 5 % of the total organic aerosol, and correlates with BC (Pr = 0.75) and other anthropogenic markers such as NO_3 (Pr = 0.94), NO_x (Pr = 0.71), and CO (Pr = 0.76). The contribution of HOA species remains at ~10% ± 2%, throughout the experiment and correlates well with BC (Pr = 0.89). As mentioned earlier, these correlations represent those that are calculated during the start of the ML sampling period. Correlations listed in Table S1 and S3 are calculated over the entire period.

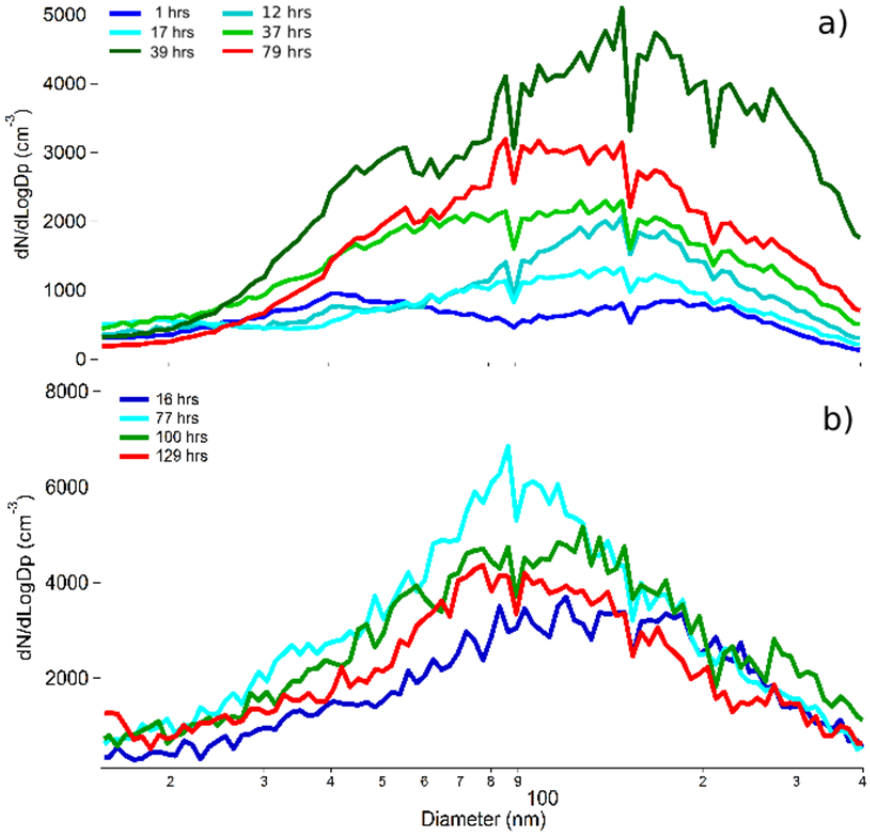

Fig. 4. Size distributions measured in the FT (a) and in the ML (b) at the PUY station. Different colours indicate sampling times extended over the sampling period, with colours ranging from blue to red as time increases.

Gas-phase measurements within the ML at the start of the sampling period are characterised by low ozone (40 and 45 ppbv), and high CO (150 and 200 ppbv) concentrations (Fig. 3(c)). The photochemical age of the sampled air mass was estimated using the NO_Y/CO and was always < 0.01, which is typical of aged air masses (Stohl *et al.*, 2002). VOC measurements shows that Benzene and Toluene contribute the largest fractions of the measured VOC species, 55% and 25%, respectively, followed by o–xylene (10%), and ethylebenzene (~5%), and p-xylene (Fig. S7). Only a small contribution from biogenic VOC (Isoprene, methylcrolein, methyletylketone, and monoterpenes) species was observed.

Initial Free Tropospheric Particle and Gas-Phase Properties

Aerosol properties measured at the start of the sampling period within the FT provided us with information on the physical and chemical properties of FT aerosol particles, prior to a sustained continental air mass. The following description on aerosol characteristics represent those measured over the initial two days of sampling. The size distribution of aerosol particles measured by the SMPS is characterised by a bimodal distribution, with a predominant fine mode at 40 ± 20 nm, and a second mode at 160 ± 20 nm (Fig. 3). The fine mode aerosol particles are likely produced within the FT by new particle formation events (Rose *et al.*, 2015). The second larger accumulation mode, is representative of aged aerosols transported over long distances (Andrews *et al.*, 2011).

The measured aerosol mass concentration (PM_1) is < 5 μg m^{-3} (Fig. (2)). Sulphate and organic aerosol particles are the major contributors to the sub-micron mass (44% and 40%, respectively). Nitrate particle mass concentration in FT is 0.1 ± 0.04 μg m^{-3} and BC mass remains at low concentrations of < 0.1 μg m^{-3}. These observations are consistent with findings by Murphy *et al.* (2006) who measured high fractions of organic and sulphur containing particles in the free troposphere. From the inorganic mass concentrations measured by the C-ToF-AMS, the ratio of the measured NH_4 to that predicted from the measured inorganic ions (NH_{4MEAS}:NH_{4PRED}) is proximately 0.68 when the site was in the FT, suggesting that the aerosol is slightly acidic (Middlebrook *et al.*, 2012). The extent to which aerosol sulphate is neutralized can be important for heterogeneous chemistry (Fan and Jacob, 1992) and ice cloud nucleation (Abbatt *et al.*, 2006; Eastwood *et al.*, 2009), and can have implications for aerosol radiative forcing (Martin *et al.*, 2004). The organic aerosol mass is made up of 60% of LV-OOA, contributions of SV-OOA and BBOA to the total organic aerosol always remain less than 10 and 20% respectively (Fig. S2(b)).

Gas-phase measurements at the site equally demonstrate characteristic properties of FT air masses (Fig. 2). In the FT, high concentrations of ozone (> 40 ppbv) and low concentrations of CO (< 150 ppbv) are observed. The ratio of NO_Y/CO, a much used means of determining air mass age (Zellweger *et al.*, 2003; Zanis *et al.*, 2007) had values < 0.005 (Fig. 3). These values are consistent with those previously measured in the FT (Zellweger *et al.*, 2003). In addition, the total measured concentrations of VOC species in the FT are approximately half that observed in the ML (Fig. S7).

Changes of Aerosol Chemical and Physical Properties in the Free Troposphere

During the persistent cold event, the continuous input of fresh pollution and constant continental air masses caused an increase in aerosol mass in the ML (Fig. 5). We observe in parallel, continuous changes to the aerosol properties in the FT. Using the MLH calculations together with the specific criteria defined in the section "*Defining Mixing Layer and Free Troposphere Measurements*", a series of FT sampling events (Table 1) provided us with an excellent opportunity to examine how the FT properties changed over a short period of time.

For the aerosol size distributions we observe a continuing

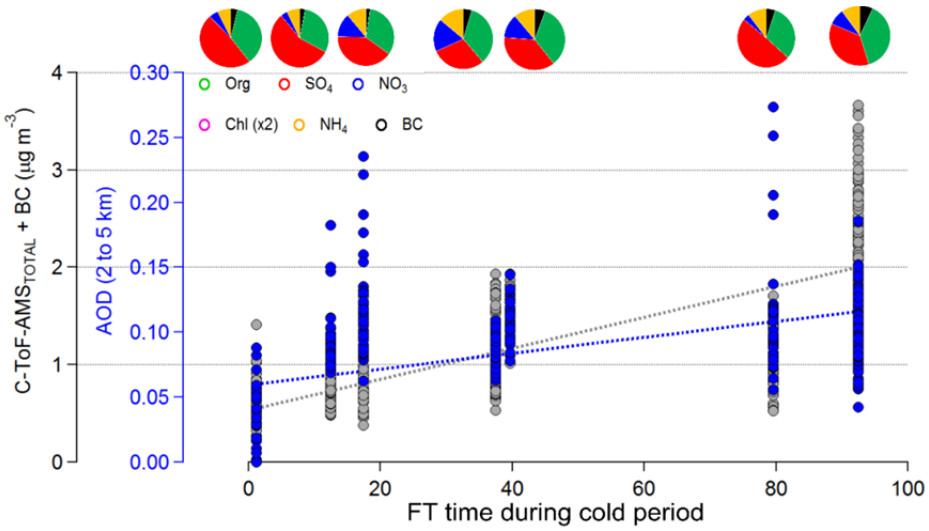

Fig. 5. Increase in total aerosol mass over time as well the corresponding AOD values calculated using the LIDAR measurements.

Table 1. Linear fitting parameters from Eq. (3), representing the observed increases in aerosols properties during the period of study. Errors are ± 1σ. Given the large number of points used for these correlations, any correlations with Pr-value ≥ 0.10 are considered significant to 0.05 (Pearsons two-tailed test).

X_i	α	β	r
$X_i = \alpha\,(Hrs) + \beta$ Eq. (5)			
$Mass_{FT}$	0.016 ± 0.001	0.54 ± 0.025	0.78
Org_{FT}	0.009 ± < 0.001	0.31 ± 0.015	0.78
SO_{4FT}	0.005 ± < 0.001	0.58 ± 0.02	0.51
NO_{3FT}	0.002 ± < 0.001	0.10 ± 0.007	0.51
CCN_{FT}	1.1 ± 0.08	343 ± 4	0.25
CN_{FT}	–2.4 ± 3.2	805 ± 7	–0.57
K_{FT}	–0.001 ± < 0.0001	0.4– ± 0.001	–0.71
AOD_{FT}	0.06 ± 0.02	0.0006– ± 0.0003	0.66
ΔF_{FT}	–0.002 ± 0.003	–1.4 ± 0.203	–0.24
EXT_{FT}	0.11 ± 0.03	3.34 ± 1.39	0.87
$Mass_{ML}$	0.102 ± 0.04	2.36 ± 2.69	0.65
CCN_{ML}	6.9 ± 5.8	637 ± 351	0.44
CN_{ML}	15 ± 10.3	1239 ± 622	0.52

increase in the contribution of the larger mode aerosol particles (> 100 nm) as the cold period persists, but the smaller mode (< 100 nm) remains the same (Fig. 4). The increase in the accumulation mode particles is likely a result of aerosols transported from the ML. However, the lack of changes in the fine mode would indicate that new particle formation in the FT occurs with the same frequency over the course of the cold period. This is consistent with observations by Rose *et al.* (2015). No significant changes in the modal average geometric mean diameter are measured in the size distribution of ML aerosol particles (Fig. 4).

In addition to changes in aerosol size distributions, several changes in aerosol physical and chemical properties were observed over the period of study. In order to determine the change in these properties as a function of time, a linear fit was performed through these properties as a function of accumulated hours in the FT or in the ML (Eq. (5)).

$$X_i = \alpha\,(Hrs) + \beta \quad (5)$$

where, X represents the concentration of species (*i*) after a number of hours (Hrs) in the FT. Values for α and β are decided from linear fits of the variable concentrations as a function of time in the FT. The number of accumulated hours in the FT was calculated by adding the hours of sampling since the first period of FT sampling. The resulting fits, the error ± 1σ, and the correlation (r) for different aerosol properties are listed in Table 1. Total aerosol mass concentration increased gradually in the FT (Fig. 5). For the total aerosol mass concentration ($Mass_{FT}$), the resulting fit shows that every 24 hours, the total aerosol mass can increase by 0.37 ± 0.022 μg m^{-3}. Heald *et al.* (2005) observed high concentrations of aerosols during airborne measurements in the FT, values 10 to 100 times greater than those used in global transport models. It was estimated that with a uniform increase in concentration of 4 μg m^{-3} instead of < 2 μg m^{-3} throughout the FT column an increase in aerosol optical depth of 0.057 at 550 nm is possible, and would result in a top of column radiative forcing of –1.2 Wm^{-2}. Therefore, our observations showing a gradual and consistent increase in aerosol mass is likely to have a significant influence on aerosol radiative forcing. The increase in aerosol particle mass concentrations during the cold event was principally composed of increases in the organic aerosol particles from 0.69 ± 0.2 μg m^{-3} up to 1.42 ± 0.3 μg m^{-3} and of NO_3 aerosol particles from 0.09 ± 0.04 μg m^{-3} up to 0.32 ± 0.11 μg m^{-3}, respectively. The increase in both the Org and NO_3 concentrations is evidence of anthropogenic aerosols being transported from the ML to the FT (Fig. 5). The change in aerosol mass concentration as a function of accumulated hours in the FT, included increases of about 0.15 ± 0.01 μg m^{-3} and 0.03 ± 0.03 μg m^{-3} per day of organic and nitrate species respectively during stable meteorological conditions. In comparison, an increase in the total mass of aerosols in the ML is as large as 2.44 ± 0.77 μg m^{-3} over a 24 hour period (Eq. (5), Table 1).

Although the total organic aerosol increased in the FT, the contribution of each type of organic aerosol did not vary significantly. The BBOA and HOA had small increases in concentrations from 0.07 ± 0.04 μg m^{-3} up to 0.16 ± 0.03 μg m^{-3} and 0.025 ± 0.01 μg m^{-3} up to 0.062 ± 0.02 μg m^{-3}, respectively over the period of the study. Similar increases were observed for both LV-OOA and SV-OOA aerosol particles that increased from 0.15 ± 0.05 μg m^{-3} up to 0.38 ± 0.08 μg m^{-3} and from 0.03 ± 0.02 μg m^{-3} to 0.16 ± 0.05 μg m^{-3}, respectively. These increases were relatively small compared to those in the ML where BBOA, SVOOA, and LV-OOA increased from 0.067 μg m^{-3} ± 0.03 up to 0.67 ± 0.47 μg m^{-3}, 0.03 ± 0.02 μg m^{-3} up to 0.46 ± 0.32 μg m^{-3} and 0.14 ± 0.05 μg m^{-3} up to 0.67 ± 0.48 μg m^{-3}, respectively. The concentration of HOA aerosol within the ML remained constant over the period of sampling.

Increases in gas-phase species such as NO_2 (from 1.05 ppb to 1.58 ppb), and NO (0.32 to 0.86 ppb) were also observed in the FT, SO_2 concentrations increased from 0.74 ± 0.6 up to 0.81 ± 0.05 ppb. Once NO_x species enter into the FT, dry deposition no longer occurs and their lifetime can increase significantly. Despite the doubling of the NO_x concentrations,

only small increases in ozone and CO were observed during this event, with O_3 increasing from 49 ± 1.7 ppb up to 51 ± 0.2 ppb, and CO increased from 142 ± 16 ppb up to 146 ± 5 ppb. The measured anthropogenic aromatic compounds (benzene, toluene, heptane, and ethylbenzene) increased in the FT during the cold event by a factor of 8, 2.5, 3.7, and 1.8 respectively. The CO/NO_x ratio decreased from 121 ± 37 down to 62 ± 7 over the time period within the free troposphere, again confirming that during this cold period fresh polluted air masses are being transported into the FT from the ML. Within the ML, the CO increased from 129 ± 16 ppb up to 212 ± 46 ppb and O_3 decreased from 48 ± 0.32 ppb down to 34 ± 10 ppb. NO_x changed from 2.1 ± 1.3 ppb to 6.3 ± 3 ppb.

Influence of Cold Period on Aerosol Direct and Indirect Radiative Properties

Direct Effects

The measured absorption coefficient (σ_{ABS} at 355 nm) of the aerosol particles in the ML was 1.6 ± 0.48 Mm^{-1} at the start of the cold event, which is within the normal range of values measured at the PUY site throughout the year (Hervo *et al.*, 2014). However, as the cold event persisted and the concentrations of aerosol particles increased, the measured σ_{ABS} increased to > 4 Mm^{-1}. Values greater than 2 Mm^{-1} are considered to be representative of polluted conditions, as is often reported at Mont Cimone in Italy (Andrews *et al.*, 2011). The σ_{ABS}, measured within the FT at the start of the cold event had mean values of 0.46 ± 0.09 Mm^{-1}, similar to those measured at other high altitude sites around Europe, such as Jungfrahjoch and Izana (~0.5 Mm^{-1}) (Andrews *et al.*, 2011). However, as the cold event persisted, the σ_{ABS} increased to values > 1.5 Mm^{-1}, almost similar to values measured in the ML at the start of the cold event, and more than doubling of aerosol absorption properties within the FT over the course of the cold event.

Aerosol scattering (σ_{SCAT}) coefficients in the ML measured by the nephelometer were 11 ± 4 Mm^{-1} at 550 nm, and increased to values > 30 Mm^{-1} over the course of the cold period within the ML. Within the FT, σ_{SCAT} coefficients were much lower with mean values of ~3.4 ± 0.6 Mm^{-1} at the start of the cold period, but increased to values of 14 ± 5 Mm^{-1} over the cold period. The resulting atmospheric extinction (EXT) (absorption + scattering) of FT aerosols showed a significant increase in values from 4 Mm^{-1} up to 16 Mm^{-1}, the linear fit through this data (Table 1) suggests that the extinction will increase by 3 ± 2 Mm^{-1} every 48 hours. This increase in atmospheric extinction by aerosol particles in the FT would result in a considerable reduction in the net solar radiation reaching the earth.

The single scattering albedo (ω0), was calculated using both absorption and scattering measurements from a 3-wavelength (450, 550, 700 nm) nephelometer. The errors in these measurements are estimated to be approximately 10% and 15% for absorption and scattering, respectively. These errors are estimated from calibrations, truncation errors for the scattering coefficient, and from noise. More details of these calculations can be found in Hervo *et al.* (2012). The value of ω0 did not vary considerably over the measurement period in the FT, with mean values of 0.88 ± 0.02. Similarly, within the ML, the ω0 also remained table with a mean value of 0.89 ± 0.01, showing that the intrinsic optical properties of the aerosol did not change greatly over the cold period.

The optical properties measured at the PUY site can be used to quantify the radiative impact of the measured aerosol through calculating the radiative efficiency (ΔE) of the aerosol (Chlek and Wong, 1995) (Eq. (6)). The ΔE allows us to compare the radiative impact of aerosol particles using the physical properties of the measured aerosol particles independent of the quantity of aerosols present (τ) and can be defined as:

$$\Delta E = \frac{\Delta F}{\tau} = -\frac{S_O}{4} T_{atm^2} \left(1 - N_{cloud}\right) 2\left[\left(1-a\right)^2 \beta_r \omega 0 - 2a\left(1-\omega 0\right)\right] \quad (6)$$

where S_O is the solar constant, T_{atm} is the transmittance of the atmosphere over the aerosol layer (0.79), N_{cloud} is the fraction of the sky covered by clouds and is set to 0 for this calculation, τ is the optical thickness, ω0 is the single scattering albedo and βr is the aerosol scatter fraction (Bond and Bergstrom, 2006; Andrews *et al.*, 2011). ΔE of the FT aerosol was determined to be –38 Wm^{-2} τ^{-1} ± 5 Wm^{-2} τ^{-1}, and increased slightly (although within the measurement error) to approximately –34 ± 1.5 Wm^{-2} τ^{-1} over the course of the cold period.

The radiative forcing (ΔF) of the aerosol is more often used when describing aerosol optical properties, and describes the total radiative impact of aerosol due to both the increase of aerosol mass loading and changes to aerosol optical properties. However, in order to quantify the radiative forcing of the changes in aerosol properties (under cloud free conditions) it is necessary to know the aerosol optical depth (AOD). As described in section on optical measurements, the AOD was calculated between 2 and 5 km from LIDAR. Using a linear fit through the AOD measurements (Fig. 5) as a function of time (Table 1) we observe that over a 48 hour period the AOD values increases by 0.05 ± 0.014, which should result in a net cooling of the atmosphere. This change is similar to that predicted (0.057) by Heald *et al.* (2005), for a doubling of aerosol mass loadings in the FT. These values were then used together with the ΔE to determine the aerosol radiative forcing. We observe that the radiative forcing decreases from –0.9 ± 0.4 Wm^{-2} to –1.3 ± 0.3 Wm^{-2} The variation in these measurements do not allow us to conclude whether there is a definite increase/decrease over the period of 7 days in the FT. For more concrete results it would be necessary to perform a radiative forcing model calculation. We feel however that this is outside the scope of the current work.

Indirect Effects

Asmi *et al.* (2012) showed that aerosol hygroscopicity (κ-values) can be accurately calculated using a combination of aerosol chemistry measurements and Köhler theory. We

therefore calculate κ-values from the aerosol chemistry measured by the C-ToF-AMS instrument. The mass factions of the inorganic, organic, and BC ions were measured by the C-ToF-AMS and MAAP instruments were converted to volume factions using a density of 1.3 g cm^{-3} for organics, 1.75 g cm^{-3} for inorganic, and 1.8 g cm^{-3} for BC. A κ-value of 0.61 was used for the inorganic species (calculated using the ZSR mixing rule (Stokes and Robinson, 1966) and a value of 0.28 was used for the organic species (Eq. (7)). A κ-value of 0.28 for organics was calculated by Asmi *et al.* (2012) using closure between chemistry and cloud condensation measurements during the same period.

$$\kappa = V_{inorg} \cdot 0.61 + V_{org} \cdot 0.28 + V_{bc} \cdot 0 \quad (7)$$

During the study period, the κ_{pred} varied between 0.40 and 0.48. These values are similar to those values measured with a cloud condensation nuclei chamber (CCNC) at the site earlier on in the month of February 2012 (Asmi *et al.*, 2012), as well as with those calculated from hygroscopicity measurements (Holmgren *et al.*, 2014). The κ_{pred} calculated from the measured aerosol chemistry in the FT, shows high values of approximately 0.47 ± 0.05. However, as a result of the increased contribution of organic aerosol in the FT, the κ_{pred} gradually decreased to 0.42 ± 0.03 (Fig. 6). Using the chemistry derived κ-values we determined the critical diameters required for an aerosol to become a cloud droplet (D_{50}) from Eq. (8) (Petters and Kreidenweis, 2007).

$$S\left(D_p\right) = \frac{D_p^3 - D_{p50}^3}{D_p^3 - D_{p50}^3\left(1-\kappa\right)} exp\left(\frac{4\sigma_w M_w}{RT\sigma_w D_P}\right) \quad (8)$$

where S represents the saturation ratio (S is the same as the RH at sub-saturated regime, e.g., S = 0.9 while RH = 90%), σ_w is the surface tension of water, M_w is the molecular weight of water, ρw is the density of water, R is the universal gas constant, T is the temperature (298 K) and D_0 is the diameter of dry particle. A saturation ratio, S, of 0.24% was used since this was shown to be representative of the average super-saturation of the clouds at the PUY station (Asmi *et al.*, 2012). The calculated Dp50 data together with the SMPS were then used to calculate the number of potential CCN during the measurement period.

The mean CCN values, at the start of the cold period within the FT_{START}, were 294 ± 84 cm^{-3} and total CN concentrations were 953 ± 330 cm^{-3}, giving a corresponding fraction activated (F_{ACT}) of 31 ± 1%. CCN and CN concentrations in ML_{START} were higher at 1388 ± 225 cm^{-3} and 1952 ± 444 cm^{-3}, respectively, resulting in a corresponding F_{ACT} of 68 ± 7%. The slightly lower F_{ACT} in the FT is linked to the high contribution of particles with diameters < 80 nm. In the FT, the CCN number increased in concentration by the end of the cold period to mean values of 449 ± 56 cm^{-3} (Fig. 6) and total CN concentrations remained the same within error having mean values of 829 ± 94 cm^{-3}. The resulting F_{ACT} quickly increased up to 54 ± 1% at the end of the cold event. The increased F_{ACT} of the aerosol particles in the FT is mainly related to the increase in the number concentration of larger accumulation mode particles observed in Fig. 3. Using the linear fits through the data (Table 1), we determine that over a 72-hour period there would be a 34 ± 15% increase in the CCN concentrations. Therefore resulting in an increase in cloud albedo. Within the ML, both the CCN and CN (Eq. (5) and Table 1) concentrations increased together so that the F_{ACT} remained the same throughout the period at 54 ± 6%.

CONCLUSIONS

An intensive field campaign took place at the regional altitude PUY research site during the month of February 2012. The measurement site was equipped with an extensive range of measurements including gas and particle phase chemistry, aerosol size distributions, and aerosol optical properties, all with a time resolution of approximately 5

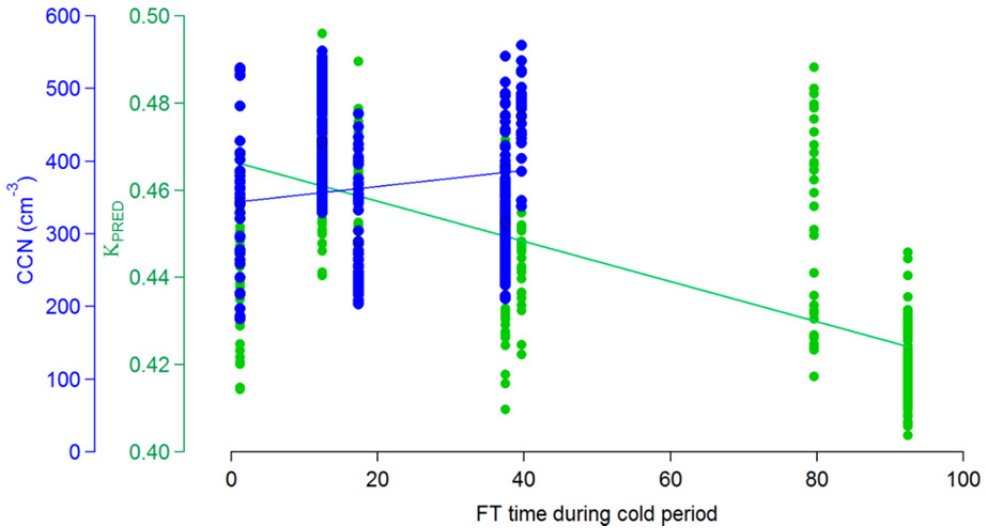

Fig. 6. Changes in the number of CCN and in the aerosol hygroscopicity parameter K, in the free troposphere over the course of the cold period. Error bars represent ± 1σ.

minutes. These in-situ measurements were complemented with vertical measurements of atmospheric back scattering with a LIDAR instrument. During this time, an exceptionally cold and dry meteorological period was encountered over the whole of Europe, leading to an exceptional increase in the operations of gas and coal stations around Europe. Depending on the height of the aerosol mixing layer (confirmed by LIDAR measurements), the PUY station was either sampling in the ML or in the FT, providing us with an excellent opportunity to study aerosol particle properties in two different atmospheric layers. Aerosol composition within the ML was composed predominantly of nitrate and organic aerosols. Unconstrained PMF analysis of the organic aerosol allowed us to identify sources of organic aerosol including biomass burning and traffic emissions, alongside regional oxidised organic aerosols. As a result of the meteorological conditions, we were able to characterise trace gases and aerosol properties within the FT and observe how these properties change as a function of time during the cold event. Increases in the larger accumulation mode of aerosol size distributions as well as increased number concentrations were observed leading to an increased number of potential CCN. The CCN concentrations increased by up to 34% over the course of a 72-hour period, suggesting a gradual influence on aerosol indirect effects. In addition to changes in the aerosol size distribution, aerosol mass measured in the FT over the course of the cold event increased by a factor of 2. The chemical composition of FT aerosol particles changed with an enrichment of nitrate (factor of 3.6) and organic (factor of 2) compounds. These measurements suggest that the FT air masses were gradually fed with ML aerosols during this period. This hypothesis was strengthened by the observed decrease in the chemical age of the FT air masses.

Measurements of aerosol optical properties, allowed us to calculate the atmospheric extinction (EXT) by aerosol particles. These properties showed a gradual increase in EXT from 4 Mm^{-1} up to 16 Mm^{-1} with time in the FT. The calculated change in AOD (+0.05) and the decrease in ΔF from –0.9 to –1.3 Mm^{-1}, together with the increasing CCN number concentrations suggest that the transport of pollutants over long distances potentially results in the cooling of the FT regional atmosphere. The results of these measurements can be used to improve the current understanding of how transported anthropogenic emissions can influence aerosol direct and indirect effects.

ACKNOWLEDGEMENTS

This work was performed in the framework of the Research Infrastructure Action under the FP6 Structuring the European Research Area Program, EUSAAR Contract No. RII3-CT-2006-026140, and ACTRIS (Aerosols, Clouds and Trace gases Research Infra Structure Network). It was supported by the LEFE/DFG program within the project "Secondary organic aerosol production in the lower troposphere over western Europe" and a Marie-Curie IRG grant (ACI-AMS). We thank the ECMWF organization for access to ERA-interim reanalysis. We would also wish to acknowledge the work of the technical staff within the laboratory who are involved in the maintenance of the Puy de Dome station, and the operation of the LIDAR instrument at the Cezeaux site.

REFERENCE

Abbatt, J.P.D., Benz, S., Cziczo, D.J., Kanji, Z., Lohmann, U. and Moehler, O. (2006). Solid Ammonium Sulfate Aerosols as Ice Nuclei: A Pathway for Cirrus Cloud Formation. *Science* 313: 1770–1773.

Anderson, T.L. and Ogren, J.A. (1998). Determining Aerosol Radiative Properties Using the TSI 3563 Integrating Nephelometer. *Aerosol Sci. Technol.* 29: 57–69.

Andrews, E., Sheridan, P.J., Fiebig, M., McComiskey, A., Ogren, J.A., Arnott, P., Covert, D., Elleman, R., Gasparini, R., Collins, D., Jonsson, H., Schmid, B. and Wang, J. (2006). Comparison of Methods for Deriving Aerosol Asymmetry Parameter. *J. Geophys. Res.* 111: D05S04, doi: 10.1029/2004JD005734.

Andrews, E., Ogren, J.A., Bonasoni, P., Marinoni, A., Cuevas, E., Rodríguez, S., Sun, J.Y., Jaffe, D.A., Fischer, E.V., Baltensperger, U., Weingartner, E., Coen, M.C., Sharma, S., Macdonald, A.M., Leaitch, W.R., Lin, N.H., Laj, P., Arsov, T., Kalapov, I., Jefferson, A. and Sheridan, P. (2011). Climatology of Aerosol Radiative Properties in the Free Troposphere. *Atmos. Res.* 102: 365–393.

Asmi, A., Wiedensohler, A., Laj, P., Fjaeraa, A.M., Sellegri, K., Birmili, W., Weingartner, E., Baltensperger, U., Zdimal, V., Zikova, N., Putaud, J.P., Marinoni, A., Tunved, P., Hansson, H.C., Fiebig, M., Kivekäs, N., Lihavainen, H., Asmi, E., Ulevicius, V., Aalto, P.P., Swietlicki, E., Kristensson, A., Mihalopoulos, N., Kalivitis, N., Kalapov, I., Kiss, G., de Leeuw, G., Henzing, B., Harrison, R.M., Beddows, D., O'Dowd, C., Jennings, S.G., Flentje, H., Weinhold, K., Meinhardt, F., Ries, L. and Kulmala, M. (2011). Number Size Distributions and Seasonality of Submicron Particles in Europe 2008-2009. *Atmos. Chem. Phys.* 11: 5505–5538.

Asmi, E., Freney, E., Hervo, M., Picard, D., Rose, C., Colomb, A. and Sellegri, K. (2012). Aerosol Cloud Activation in Summer and Winter at Puy-de-Dome High Altitude Site in France. *Atmos. Chem. Phys.* 12: 11589–11607.

Bond, T.C. and Bergstrom, R.W. (2006). Light Absorption by Carbonaceous Particles: An Investigative Review. *Aerosol Sci. Technol.* 40: 27–67.

Brooks, I.M. (2003). Finding Mixing Layer Top: Application of a Wavelet Covariance Transform to Lidar Backscatter Profiles. *J. Atmos. Oceanic Technol.* 20: 1092–1105.

Crippa, M., Canonaco, F., Lanz, V.A., Äijälä, M., Allan, J.D., Carbone, S., Capes, G., Ceburnis, D., Dall'Osto, M., Day, D.A., DeCarlo, P.F., Ehn, M., Eriksson, A., Freney, E., Hildebrandt Ruiz, L., Hillamo, R., Jimenez, J.L., Junninen, H., Kiendler-Scharr, A., Kortelainen, A.M., Kulmala, M., Laaksonen, A., Mensah, A.A., Mohr, C., Nemitz, E., O'Dowd, C., Ovadnevaite, J., Pandis, S.N., Petäjä, T., Poulain, L., Saarikoski, S., Sellegri, K., Swietlicki, E., Tiitta, P., Worsnop, D.R., Baltensperger, U. and Prévôt, A.S.H. (2014). Organic Aerosol Components Derived

from 25 AMS Data Sets across Europe Using a Consistent ME-2 Based Source Apportionment Approach. *Atmos. Chem. Phys.* 14: 6159–6176.

Chaumerliac, N., Rosset, R., Renard, M. and Nickerson, E.C. (2004). The Transport and Redistribution of Atmospheric Gases in Regions of Frontal Rain. *J. Atmos. Chem*. 14: 43–51.

Clain, G., Baray, J.L., Delmas, R., Keckhut, P. and Cammas, J.P. (2010). A Lagrangian Approach to Analyse the Tropospheric Ozone Climatology in the Tropics: Climatology of Stratosphere - Troposphere Exchange at Reunion Island. *Atmos. Environ.* 44: 968–975.

Crumeyrolle, S., Schwarzenboeck, A., Roger, J.C., Sellegri, K., Burkhart, J.F., Stohl, A., Gomes, L., Quennehen, B., Roberts, G., Weigel, R., Villani, P., Pichon, J.M., Bourrianne, T. and Laj, P. (2013). Overview of Aerosol Properties Associated with Air Masses Sampled by the ATR-42 during the EUCAARI Campaign (2008). *Atmos. Chem. Phys.* 13: 4877–4893, doi: 10.5194/acp-13-4877-2013.

Chylek, P. and Wong, J. (1995). Effect of Absorbing Aerosols on Global Radiative Budget. *Geophys. Res. Lett.* 22: 929–931.

Das, S.K. and Jayaraman, A. (2012). Long-Range Transportation of Anthropogenic Aerosols over Eastern Coastal Region of India: Investigation of Sources and Impact on Regional Climate Change. *Atmos. Res.* 118: 68–83, doi: 10.1016/j.atmosres.2012.05.025.

Donnell, EA., Fish, D.J., Dicks, E.M. and Thorpe, A.J. (2001). Mechanisms for Pollutant Transport between the Mixing Layer and the Free Troposphere. *J. Geophys. Res.* 106: 7847–7856, doi: 10.1029/2000JD900730.

Drewnick, F., Hings, S.S., DeCarlo, P., Jayne, J.T., Gonin, M., Fuhrer, K., Weimer, S., Jimenez, J.L., Demerjian, K.L., Borrmann, S. and Worsnop, D.R. (2005). A New Time-of-Flight Aerosol Mass Spectrometer (ToF-AMS) – Instrument Description and First Field Deployment. *Aerosol Sci. Technol.* 39: 637–658.

Eastwood, M.L., Cremel, S., Wheeler, M., Murray, B.J., Girard, E. and Bertram, A.K. (2009). Effects of Sulfuric Acid and Ammonium Sulfate Coatings on the Ice Nucleation Properties of Kaolinite Particles. *Geophys. Res. Lett.* 36: L02811.

Fan, S. and Jacob, D. (1992). Surface Ozone Depletion in Artic Spring Sustained by Bromine Reactions. *Nature* 359: 522–524.

Fiedler, F. (1982). Atmospheric Circulation. In *Chemistry of the Unpolluted and Polluted Troposphere*, Georgii, H.W. and Jaeschke, W. (Eds.), p. 509, Reidel Publishing Company, Dordrecht.

Froyd, K.D., Murphy, D.M., Sanford, T.J., Thomson, D.S., Wilson, J.C., Pfister, L. and Lait, L. (2009). Aerosol Composition of the Tropical Upper Troposphere. *Atmos. Chem. Phys.* 9:4363–4385.

Freney, E.J., Sellegri, K., Canonaco, F., Boulon, J., Hervo, M., Weigel, R., Pichon, J.M., Colomb, A., Prévôt, A.S.H. and Laj, P. (2011). Seasonal Variations in Aerosol Particle Composition at the Puy-de-Dôme Research Station in France. *Atmos. Chem. Phys.* 11: 13047-13059, doi: 10.5194/acp-11-13047-2011

Freville, P., Montoux, N., Baray, J.L., Chauvigne, A., Reveret, F., Hervo, M., Dionisi, D., Payen, G. and Sellegri, K. (2015). LIDAR Developments at Clermont-Ferrand-France for Atmospheric Observation. *Sensors* 15: 3041-69. doi: 10.3390/s150203041.

Heald, C.L., Jacob, D.J., Park, R.J., Russell, L.M., Huebert, B.J., Seinfeld, J.H., Liao, H. and Weber, R.J. (2005). A Large Organic Aerosol Source in the Free Troposphere Missing from Current Models. *Geophys. Res. Lett.* 32: L18809, doi: 10.1029/2005GL023831.

Heald, C.L., Jacob, D.J., Turquety, S., Hudman, R.C., Weber, R.J., Sullivan, A.P., Peltier, R.E., Atlas, E.L., de Gouw, J.A., Warneke, C., Holloway, J.S., Neuman, J.A., Flocke, F.M. and Seinfeld, J.H. (2006). Concentrations and Sources of Organic Carbon Aerosols in the Free Troposphere over North America. *J. Geophys. Res.* 111: D23S47, doi: 10.1029/2006JD007705.

Henne, S., Furger, M., Nyeki, S., Steinbacher, M., Neininger, B., de Wekker, S.F.J., Dommen, J., Spichtinger, N., Stohl, A. and Prévôt, A.S.H. (2004). Quantification of Topographic Venting of Mixing Layer Air to the Free Troposphere. *Atmos. Chem. Phys.* 4: 497–509, doi: 10.5194/acp-4-497-2004.

Hervo, M., Quennehen, B., Kristiansen, N.I., Boulon, J., Stohl, A., Fréville, P., Pichon, J.M., Picard, D., Labazuy, P., Gouhier, M., Roger, J.C., Colomb, A., Schwarzenboeck, A. and Sellegri, K. (2012). Physical and Optical Properties of 2010 Eyjafjallajökull Volcanic Eruption Aerosol: Ground-Based, Lidar and Airborne Measurements in France. *Atmos. Chem. Phys.* 12: 1721–1736.

Hervo, M., Sellegri, K., Pichon, J.M., Roger, J.C. and Laj, P. (2014). Long Term Measurements of Optical Properties and Their Hygroscopic Enhancement. *Atmos. Chem. Phys. Discuss.* 14: 27731–27767.

Holmgren, H., Sellegri, K., Hervo, M., Rose, C., Freney, E., Villani, P., and Laj, P. (2014). Hygroscopic Properties and Mixing State of Aerosol Measured at the High-altitude Site Puy de Dôme (1465 m a.s.l.), France. *Atmos. Chem. Phys.* 14: 9537–9554, doi: 10.5194/acp-14-9537-2014.

Hov, Ø. and Flatøy, F. (1997). Convective Redistribution of Ozone and Oxides of Nitrogen in the Troposphere over Europe in Summer and Fall. *J. Atmos. Chem*. 28: 319–337.

IPCC: Climate Change (2013). The Physical Science Basis, Contribution of Working Group I to the Fifth Assessment of the Intergovernmental Panel on Climate Change, Cambridge Univ. Press, United Kingdom and NY, USA, 2014.

Klett, J.D. (1981). Stable Analytical Inversion Solution for Processing LIDAR Returns. *Appl. Opt.* 20: 211–220.

Lacis, A., Wuebbles, D. and Logan, J. (1990). Radiative Forcing of Climate by Changes in the Vertical Distribution of Ozone. *J. Geophys. Res.* 95: 9971–9981.

Laj, P., Klausen, J., Bilde, M., Plaß-Duelmer, C., Pappalardo, G., Clerbaux, C., Baltensperger, U., Hjorth, J., Simpson, D., Reimann, S., Coheur, P.F., Richter, A., De Mazière, M., Rudich, Y., McFiggans, G., Torseth, K., Wiedensohler,

A., Morin, S., Schulz, M., Allan, J.D., Attié, J.L., Barnes, I., Birmili, W., Cammas, J.P., Dommen, J., Dorn, H.P., Fowler, D., Fuzzi, S., Glasius, M., Granier, C., Hermann, M., Isaksen, I.S.A., Kinne, S., Koren, I., Madonna, F., Maione, M., Massling, A., Moehler, O., Mona, L., Monks, P.S., Müller, D., Müller, T., Orphal, J., Peuch, V.H., Stratmann, F., Tanré, D., Tyndall, G., Abo Riziq, A., Van Roozendael, M., Villani, P., Wehner, B., Wex, H. and Zardini, A.A. (2009). Measuring Atmospheric Composition Change. *Atmos. Environ.* 43: 5351–5414.

Leaitch, W.R., Lohmann, U., Russell, L.M., Garrett, T., Shantz, N.C., Toom-Sauntry, D., Strapp, J.W., Hayden, K.L., Marshall, J., Wolde, M., Worsnop, D.R. and Jayne, J.T. (2010). Cloud Albedo Increase from Carbonaceous Aerosol. *Atmos. Chem. Phys.* 10: 7669–7684, doi: 10.5194/acp-10-7669-2010.

Nicolas, J., Mallet, M., Roberts, G.C., *et al.*, (2015). Aerosol Optical Properties and Instantaneous Aerosol Radiative Forcing in the Shortwave at a Local Scale over the Western Mediterranean: Airborne Observations and 1–D Radiative Transfer Model Simulations. *In Preparation for, Atmos. Chem. Phys.*

Martin, S.T., Hung, H.M., Park, R.J., Jacob, D.J., Spurr, R.J.D., Chance, K.V. and Chin, M. (2004). Effects of the Physical State of Tropospheric Ammonium-sulfate-nitrate Particles on Global Aerosol Direct Radiative Forcing. *Atmos. Chem. Phys.* 4: 183–214.

Matthais, V., Freudenthaler, V., Amodeo, A., Balin, I., Balis, D., Bösenberg, J., Chaikovsky, A., Chourdakis, G., Comeron, A., Delaval, A., De Tomasi, F., Eixmann, R., Hågård, A., Komguem, L., Kreipl, S., Matthey, R., Rizi, V., Rodrigues, J.A., Wandinger, U. and Wang, X. (2014). Aerosol Lidar Intercomparison in the Framework of the EARLINET Project. 1. Instruments. *Appl. Opt.* 43: 961–976.

McFiggans, G., Artaxo, P., Baltensperger, U., Coe, H., Facchini, M.C., Feingold, G., Fuzzi, S., Gysel, M., Laaksonen, A., Lohmann, U., Mentel, T.F., Murphy, D.M., O'Dowd, C.D., Snider, J.R. and Weingartner, E. (2006). The Effect of Physical and Chemical Aerosol Properties on Warm Cloud Droplet Activation. *Atmos. Chem. Phys.* 6: 2593–2649.

McKendry, I.G. and Lundgren, J. (2000). Tropospheric Layering of Ozone in Regions of Urbanized Complex and/or Coastal Terrain: A Review. *Prog. Phys. Geogr.* 24: 329–354.

McKendry, I.G., Hacker, J.P., Stull, R., Sakiyama, S., Mignacca, D. and Reid, K., (2001). Long-range Transport of Asian Dust to the Lower Fraser Valley, British Columbia, Canada. *J. Geophys. Res.* 106: 18361–18370.

Mills, N.L., Robinson, S.D., Fokkens, P.H., Leseman, D.L., Miller, M.R., Anderson, D., Freney, E.J., Heal, M.R., Donovan, R.J., Blomberg, A., Sandstrom, T., MacNee, W., Boon, N.A., Donaldson, K., Newby, D.E. and Cassee, F.R. (2008). Exposure to Concentrated Ambient Particles Does Not Affect Vascular Function in Patients with Coronary Heart Disease. *Environ. Health Perspect.* 116: 709–715.

Middlebrook, A.M., Bahreini, R., Jimenez, J.L. and Canagaratna, M.R. (2012). Evaluation of Composition-Dependent Collection Efficiencies for the Aerodyne Aerosol Mass Spectrometer Using Field Data. *Aerosol Sci. Technol.* 46: 258–271, doi: 10.1080/02786826.2011.620041.

Morgan, W.T., Allan, J.D., Bower, K.N., Highwood, E.J., Liu, D., McMeeking, G.R., Northway, M.J., Williams, P.I., Krejci, R. and Coe, H. (2010). Airborne Measurements of the Spatial Distribution of Aerosol Chemical Composition across Europe and Evolution of the Organic Fraction. *Atmos. Chem. Phys.* 10: 4065–4083.

Müller, D., Ansmann, A., Mattis, I., Tesche, M., Wandinger, U., Althausen, D. and Pisani, G. (2007). (2007) Aerosol-Type-Dependent Lidar Ratios Observed with Raman Lidar. *J. Geophys. Res.* 112: D16202, doi: 10.1029/2006JD008292.

Murphy, D.M., Cziczo, D.J., Froyd, K.D., Hudson, P.K., Matthew, B.M., Middlebrook, A.M., Peltier, R.E., Sullivan, A., Thomson, D.S. and Weber, R.J. (2006). Single-Particle Mass Spectrometry of Tropospheric Aerosol Particles. *J. Geophys. Res.* 111: D23S32.

Petit, J.E., Favez, O., Sciare, J., Crenn, V., Sarda-Estève, R., Bonnaire, N., Močnik, G., Dupont, J.C., Haeffelin, M. and Leoz-Garziandia, E. (2015). Two Years of near Real-time Chemical Composition of Submicron Aerosols in the Region of Paris Using an Aerosol Chemical Speciation Monitor (ACSm) and a Multi-wavelength Aethalometer. *Atmos. Chem. Phys.* 15: 2985–3005, doi: 10.5194/acp-15-2985-2015.

Petters, M.D. and Kreidenweis, S.M. (2007). A Single Parameter Representation of Hygroscopic Growth and Cloud Condensation Nucleus Activity. *Atmos. Chem. Phys.* 7: 1961–1971, doi: 10.5194/acp-7-1961-2007.

Petters, M.D., Kreidenweis, S.M. (2008). A Single Parameter Representation of Hygroscopic Growth and Cloud Condensation Nucleus Activity - Part 2: Including Solubility. *Atmos. Chem. Phys.* 8: 1680–7316.

Petzold, A., Gysel, M., Vancassel, X., Hitzenberger, R., Puxbaum, H., Vrochticky, S., Weingartner, E., Baltensperger, U. and Mirabel, P. (2005). On the Effects of Organic Matter and Sulphur-containing Compounds on the CCN Activation of Combustion Particles. *Atmos. Chem. Phys.* 5: 3187–3203, doi: 10.5194/acp-5-3187-2005.

Platnick, S. and Twomey, S. (1994). Determining the Susceptibility of Cloud Albedo to Changes in Droplet Concentration with the Advanced Very High Resolution Radiometer. *J. Appl. Meteorol.* 33: 334–347, doi: 10.1175/1520-0450(1994)033<0334:DTSOCA>2.0.CO;2

Pringle, K.J., Tost, H., Pozzer, A., Poeschl, U. and Lelieveld, J. (2010). Global distribution of the effective aerosol hygroscopicity parameter for CCN activation. *Atmos. Chem. Phys.* 10: 5241–5255.

Roberts, G.C. and Nenes, A. (2005). A Continuous-flow Streamwise Thermal-gradient CCN Chamber for Atmospheric Measurements. *Aerosol Sci. Technol.* 39: 206–221.

Rose, C., Boulon, J., Hervo, M., Holmgren, H., Asmi, E., Ramonet, M., Laj, P. and Sellegri, K. (2013). Long-term Observations of Cluster Ion Concentration, Sources and

Sinks in Clear Sky Conditions at the High-Altitude Site of the Puy de Dome, France. *Atmos. Chem. Phys.* 13: 11573–11594.

Rose, C., Sellegri, K., Asmi, E., Hervo, M., Freney, E., Colomb, A., Junninen, H., Duplissy, J., Sipilä, M., Kontkanen, J., Lehtipalo, K. and Kulmala, M. (2015). Major Contribution of Neutral Clusters to New Particle Formation at the Interface between the Boundary Layer and the Free Troposphere. *Atmos. Chem. Phys.* 15: 18355–18388.

Stohl, A., Trainer, M., Ryerson, T.B., Holloway, J.S. and Parrish, D.D. (2002). Export of NO_y from the North American Mixing Layer during 1996 and 1997 North Atlantic Regional Experiments. *J. Geophys. Res.* 107, doi: 10.1029/2001JD000519, 2002b.

Stull, R.B (1988). *An Introduction to Boundary Layer Meteorology*, Kluwer Academic Publishers.

Timonen, H., Wigder, N. and Jaffe, D. (2013). Influence of Background Particulate Matter (PM) on Urban Air Quality in the Pacific Northwest. *J. Environ. Manage.* 129: 333–340, doi: 10.1016/j.jenvman.2013.07.023.

Topping, D.O., McFiggans, G.B. and Coe, H. (2005a). A Curved Multi-component Aerosol Hygroscopicity Model Framework: Part 1 - Inorganic Compounds. *Atmos. Chem. Phys.* 5: 1205–1222.

Topping, D.O., McFiggans, G.B. and Coe, H. (2005b). A Curved Multi-component Aerosol Hygroscopicity Model Framework: Part 2 - Including Organic Compounds. *Atmos. Chem. Phys.* 5: 1223–1242.

Twohy, C.H., Clement, C.F., Gandrud, B.W., Weinheimer, A.J., Campos, T.L., Baumgardner, D., Brune, W.H., Faloona, I., Sachse, G.W., Vay, S.A. and Tan, D. (2002). Deep Convection as a Source of New Particles in the Midlatitude Upper Troposphere. *J. Geophys. Res.* 107: 4560.

Ulbrich, I.M., Canagaratna, M.R., Zhang, Q., Worsnop, D.R. and Jimenez, J.L. (2009). Interpretation of Organic Components from Positive Matrix Factorization of Aerosol Mass Spectrometric Data. *Atmos. Chem. Phys.* 9: 2891–2918.

Zanis, P., Ganser, A., Zellweger, C., Henne, S., Steinbacher, M. and Staehelin, J. (2007). Seasonal Variability of Measured Ozone Production Efficiencies in the Lower Free Troposphere of Central Europe. *Atmos. Chem. Phys.* 7: 223–236, doi: 10.5194/acp-7-223-2007.

Zellweger, C., Forrer, J., Hofer, P., Nyeki, S., Schwarzenbach, B., Weingartner, E., Ammann, M. and Baltensperger, U. (2003) Partitioning of Reactive Nitrogen (NO_y) and Dependence on Meteorological Conditions in the Lower Free Troposphere. *Atmos. Chem. Phys.* 3: 779–796, doi: 10.5194/acp-3-779-2003.

Received for review, March 22, 2015
Revised, September 22, 2015
Accepted, January 4, 2016